

Article

Prediction of Reservoir Quality from Log-Core and Seismic Inversion Analysis with an Artificial Neural Network: A Case Study from the Sawan Gas Field, Pakistan

Zhang Qiang ^{1,2,3}, Qamar Yasin ^{1,2,*} , Naser Golsanami ^{4,5}  and Qizhen Du ^{1,2} 

¹ Key Laboratory of Deep Oil and Gas, China University of Petroleum (East China), 66th Changjiang West Road, Qingdao 266580, China; zhangqiang108.slyt@sinopec.com (Z.Q.); dqz@upc.edu.cn (Q.D.)

² Laboratory for Marine Mineral Resources, Qingdao National Laboratory for Marine Science and Technology, Qingdao 266071, China

³ Research Institute of Exploration and Development, Shengli Oilfield Branch, SINOPEC, Dongying, Shandong 257015, China

⁴ State Key Laboratory of Mining Disaster Prevention and Control, Shandong University of Science and Technology, Qingdao 266590, China; golsanami_naser@yahoo.com

⁵ College of Mining and Safety Engineering, Shandong University of Science and Technology, Qingdao 266590, China

* Correspondence: qamarquaidian@gmail.com; Tel.: +86-131-5685-8552

Received: 21 December 2019; Accepted: 15 January 2020; Published: 19 January 2020



Abstract: This paper presents a novel approach that aims to predict better reservoir quality regions from seismic inversion and spatial distribution of key reservoir properties from well logs. The reliable estimation of lithology and reservoir parameters at sparsely located wells in the Sawan gas field is still a considerable challenge. This is due to three main reasons: (a) the extreme heterogeneity in the depositional environments, (b) sand-shale intercalations, and (c) repetition of textural changes from fine to coarse sandstone and very coarse sandstone in the reservoir units. In this particular study, machine learning (ML) inversion algorithm was selected to predict the spatial variations of acoustic impedance (AI), porosity, and saturation. While trained in a supervised mode, the support vector machine (SVM) inversion algorithm performed effectively in identifying and mapping individual reservoir properties to delineate and quantify fluid-rich zones. Meanwhile, the Sequential Gaussian Simulation (SGS) and Gaussian Indicator Simulation (GIS) algorithms were employed to determine the spatial variability of lithofacies and porosity from well logs and core analyses data. The calibration of the detailed spatial variations from post-stack seismic inversion using SVM and wireline logs data indicated an appropriate agreement, i.e., variations in AI is related to the variations in reservoir facies and parameters. From the current study, it was concluded that in a highly heterogeneous reservoir, the integration of SVM and GIS algorithms is a reliable approach to achieve the best estimation of the spatial distribution of detailed reservoir characteristics. The results obtained in this study would also be helpful to minimize the uncertainty in drilling, production, and injection in the Sawan gas field of Pakistan as well as other reservoirs worldwide with similar geological settings.

Keywords: Sawan gas field; 3D seismic; well logs; support vector machine

1. Introduction

The high-quality region in the reservoir is defined as “the zone of maximum commercial productivity under the currently employed technology”. This definition, itself, combines the disciplines

of geophysics, geology, and petroleum engineering for the optimum production and operative description of the reservoirs [1]. Correct identification of high-quality regions requires a thorough understanding of porosity, permeability, fluid saturation, the volume of shale, areal extent, thickness, and mechanical properties (last but not least) through the integration of seismic data, wireline log, and core data analyses [2]. To quantify the high-quality regions, reservoir modeling, from drilling to reservoir management activities, plays a vital role in understanding the reservoir behavior in three-dimensional analysis. The pre-drill design primarily depends on the geosciences techniques of sub-surface evaluation to determine the locations of better reservoir-quality rocks [3]. In general, there are two approaches used to delineate and quantify the high-grade regions: (i) sub-surface evaluation using pre/post-stack seismic, well logs, and core data analysis, (ii) interpretation of well testing and production data. The latter aims to identify the best area for optimization of hydrocarbon recovery. These distinct approaches though, can be categorized as PRE-DRILL and POST-DRILL methods, respectively.

In the past few years, the inversion of seismic data to AI (acoustic impedance) has become a common practice in industry and academia for the prediction of reservoir spatial properties. An inversion is a numerical process that utilized seismic data to extract rocks' physical properties and fluids [4]. Over the recent years, several types of algorithms have been developed for mapping AI from post-stack seismic amplitude data and further linking it to reservoir properties distribution in space [5]. Nowadays, an increase in computing power and modern technologies of acquisition, processing, and interpretation of seismic data has empowered the reservoir geophysicists to focus on machine learning, i.e., extracting AI using neural network algorithms [6–9]. The advantages of artificial neural network algorithms over traditional statistical inversions are briefly discussed in the literature [6–11].

Since inversion can perform quantitative predictions of reservoir properties, it is usually associated with such sort of limitations as tuning and interference, noise, bandwidth, and non-uniqueness is also associated with inversion [12]. Thus, the accuracy of the outcome from seismic inversion depends on the selection of the inversion method, resolution of both logging and the seismic data, and signal-to-noise ratio of the target interval [10].

In this modern era, computer-based reservoir modeling has enabled us to overcome the problem of complex spatial configurations. This is possible through dividing the reservoir volume into a 3D grid of discrete volume cells which can be used as a database to integrate all available information [13]. The information for the spatial behavior of petrophysical parameters beyond the wells can only be accessed using reservoir modeling techniques. However, if the available information is not sufficient, Gaussian algorithms are a better approach to extrapolate the reservoir interval laterally and vertically [14].

The Sawan gas field, located at the middle Indus basin in Pakistan, is one of the largest fields in the world, with proven geological reserves of 3 trillion cubic feet (TCF) and expected recovery of more than 1 TCF (Figure 1a). While discovered in 1998, its commercial production was started in 2003. On production tests, individual wells discharged more than 100 million standard ft³ (2.8 million standard m³) of gas per day. Nevertheless, most surprising factor in the Sawan gas field is the high geothermal gradient, resulting in reservoir temperatures of more than 175 °C. In the Sawan gas field, the Cretaceous sandstone of the Lower Goru Formation serves as the main reservoir unit deposited in heterogeneous shallow-marine environment from proximal delta-front settings. The Lower Goru Formation is further divided into A, B, C, and D sandstone intervals (Figure 1b). As a preliminary study, the complex and highly productive part of reservoir unit, i.e., C-sand interval, was evaluated and interpreted in this study. This selection was based on the fact that the production from C-sand interval has decreased rapidly during the past few years and has reached a state of high water cut.

In the past few years, multiple studies have been carried out to evaluate the remaining potential of the C-sand interval using modern techniques [15–17]. Recent studies performed by Ali et al. [18] and Asad and Rahim [19] indicated that model-based post-stack inversion presented good results for the spatial distribution of reservoir properties and mapping potential gas-saturated zones in the C-sand

interval. Even though the model-based inversion algorithm achieved good results, the quantification of the highly productive area was scaled relative to the whole body of the reservoir. Moreover, they were unable to tie the results with laboratory-measured reservoir parameters and production data from the Sawan gas field.

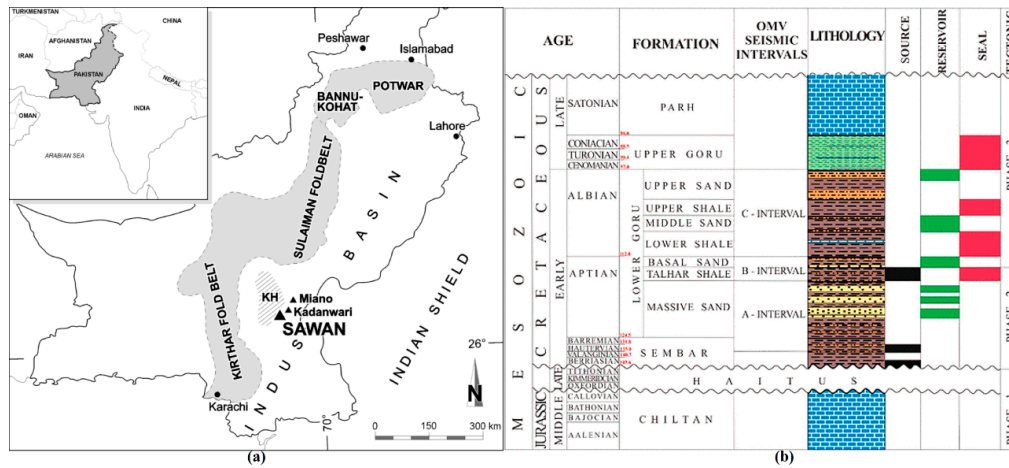


Figure 1. (a) Structural map of Pakistan with the location of the Sawan Gas Field, (b) Generalized stratigraphic column of the Lower Indus Basin with highlighted C-sand interval.

In the present study, the ML-based inversion algorithm is successfully applied in a supervised mode (with wells) to correlate the seismic attribute with porosity and saturation values. Herein, the time slices were generated at 20 ms intervals to get a better insight of the reservoir heterogeneity. The inversion slices were further correlated with lithofacies, laboratory-measured porosity data, and cross-sectional analysis of 3D effective porosity model using well logs simulation in order to map the high-quality regions in the Sawan area.

2. Materials and Methods

In this study, the well logs data from six key wells, namely A, B, C, D, E, and X were used to estimate porosity and saturation in the C-sand interval of Lower Goru Formation. The gamma-ray (GR), spontaneous potential (SP), caliper (CAL), deep resistivity (LLD), P- and S- wave sonic (DTP and DTS), density (RHOB), and neutron porosity (NPHI) logs were analyzed in order to highlight the hydrocarbon-bearing zones and reservoir modeling.

Also, 237 core samples were available from reservoir interval for comparing the reliability of porosity estimation. In this work, 3D seismic data of about 200 km² area was utilized to mark the respective stratigraphic horizons (e.g., C-sand interval of Goru Formation), as shown in Figure 2.

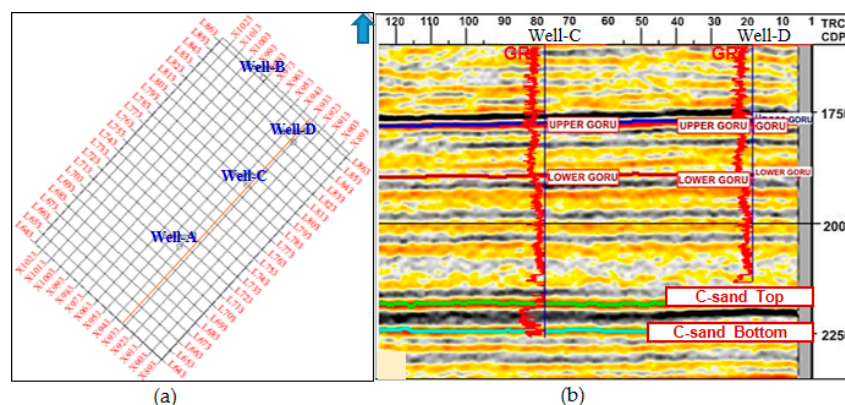


Figure 2. (a) Seismic base map with wells and Xline 932 (orange color), (b) Seismic to well tie at Xline 932.

2.1. Reservoir Parameters Estimation

In the context of the current work, the initial phase was to estimate the petrophysical parameters. This estimation was to identify the unexplored hydrocarbon-bearing zones in the reservoir interval. The following equations were employed for the estimation of effective porosity and hydrocarbon saturation.

The volume of shale (V_{sh}) was estimated from the GR log using the Equation (1):

$$V_{sh} = \frac{GR_{log} - GR_{min}}{GR_{max} - GR_{min}} \quad (1)$$

where GR_{log} , GR_{min} , and GR_{max} are gamma-ray log readings in the zone of interest, 100% clean sand, and 100% shale respectively (API units).

The total porosity was estimated using a density log by following Equation (2):

$$\varphi = \frac{\rho_{ma} - \rho_b}{\rho_{ma} - \rho_f} \quad (2)$$

where ρ_{ma} is the matrix density and ρ_f denotes fluid density.

The effective porosity (ϕ_{eff}) was estimated using the volume of shale (V_{sh}) and total porosity (ϕ) from the Equations (1) and (2):

$$\phi_{eff} = \phi_D(1 - V_{sh}) \quad (3)$$

Using Equations (1)–(3), the water saturation (S_w) was calculated using Poupone Leveaux Indonesian model:

$$S_w = \left\{ \left[\left(\frac{V_{sh}^{2-V_{sh}}}{R_{sh}} \right)^{\frac{1}{2}} + \left(\frac{\rho_e^2}{R_w} \right)^{\frac{1}{2}} \right]^2 R_t \right\}^{-1/2} \quad (4)$$

$$Sat.HC = 1 - S_w \quad (5)$$

where ' R_t ' is the true resistivity of formation taken from deep resistivity (LLD) log response, ' R_{sh} ' is the resistivity of shale (4 Ωm), ' R_w ' is the resistivity of formation water (0.5 Ωm), and *Sat. HC* is hydrocarbon saturation.

2.2. Support Vector Machine

Among the different kinds of inversion algorithms, SVM is particularly distinguished by its versatility to perform linear mapping and pattern recognition using supervised and unsupervised learning process. In the literature, the SVM has emerged as an effective inversion algorithm for complex reservoir characterization and also has been successfully adopted in a wide variety of reservoir evaluation applications from seismic to well-log data [20,21]. The main characteristic that makes the SVM a powerful ML tool is that the nonlinearly separable classes in the original feature space can be separated linearly in the higher dimensional space.

The SVM is a simple and nonlinear classifier algorithm. This algorithm essentially defines a hyper-plane that separates binary classes in a high or infinite-dimensional space. The hyper-plane is used to maximize the margins between the two classes and is determined in accordance to the subset of sample points close to the boundary called support vectors (SV) as shown in Figure 3.

For a given training vectors x_i ($i = 1, 2, \dots, n$) and two output classes = -1 or 1, SVM solves the following primal problem [22]:

$$\min_{\omega, b, \zeta} \left(\frac{1}{2} \omega^T \omega + X \sum_{i=1}^n \zeta_i \right) \quad (6)$$

$$y_i(\omega^T \varphi(x_i) + b) \geq 1 - \zeta_i \quad (7)$$

$$\text{And } \zeta_i = \max(0, 1 - y_i(\omega^T \varphi(x_i) + b)) \geq 0, i = 1, 2, \dots, n \quad (8)$$

where φ is a transformation function and ω , and b are the parameters of the linear function. The parameter X deals with the true classification of training examples versus maximization of the decision function margin. For larger values of X , a smaller margin is accepted if the decision function is better after classifying all training points correctly. In contrast, the lower values of X will satisfy a larger margin leading to a simpler decision function, at the cost of training accuracy.

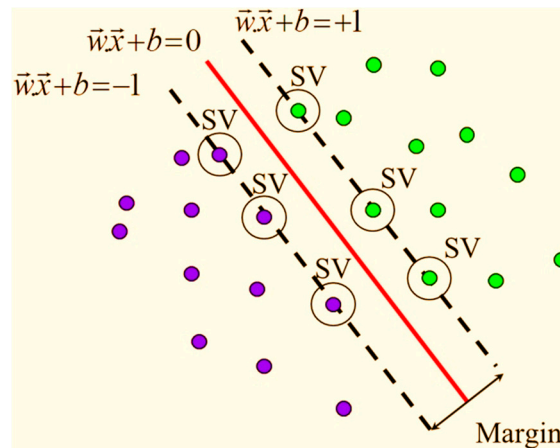


Figure 3. The diagrammatic representation of SVM for separation hyper-plane in 2D [22].

Further, a kernel trick is applied for non-linear classification problems, which maps the lower dimension feature points to higher dimension spaces as the result of which a linear separation is possible [23]. The radial basis function (RBF) is the most commonly used kernel which was also applied in the current study:

$$K(y, y') = \exp(-\gamma \|y - y'\|^2) \quad (9)$$

The kernel is managed by the kernel scale γ , which defines the influence of a single training example. The larger γ is, the closer other examples must be affected. For multi-class classification problems, one-versus-one classification is implemented to generate better classification results.

In this particular study, a computer-aided strategy using Rock Star computational software was operated for the inversion of seismic data using SVM. In Rock Star computational software, information from wells and 3D seismic cube were loaded and parameters were adjusted according to the requirements of data input.

The analyses and working procedures adopted in this study are as follows:

- Select a set of the appropriate seismic attribute after examining the seismic and well log data at well locations.
- Considering a logical relationship between suitable seismic attributes and the reservoir characters by linear or non-linear algorithms.
- Train the data until maximizing the correlation coefficient between original and synthetic AI. If the correlation is high, then apply the selected parameters information to a seismic cube and generate a cube or volume of a specific reservoir property.
- The AI model was developed to extract the petrophysical properties from seismic amplitude reflection. The results obtained from inversion was interpreted and cross-examined with other geological features to assess a prospect.

3. Results and Discussion

3.1. Reservoir Characterization from Logs and Core

The first step in reservoir characterization is to transform the raw well-bore data to reliable petrophysical properties for identifying hydrocarbon-bearing zones. Figure 4 shows log curves and

interpreted profiles of C-sand interval in Sawan gas field including porosity, water saturation, and gas content for the key wells. In the study wells, the routine core analysis data (237 core) was available to access the level of correlation between estimated and measured porosity. A good matching can be observed between measured and estimated porosity in wells C, B, and E throughout the C-sand interval (Figure 4). Note that the trend of porosity and saturation is inconsistent throughout the reservoir interval, indicating significant heterogeneities in the subject wells. Since the petrophysical interpretations show heterogeneities and complexities in the region, an extensive characterization is significant for reducing the uncertainty in drilling and improving the ultimate recovery of oil and gas.

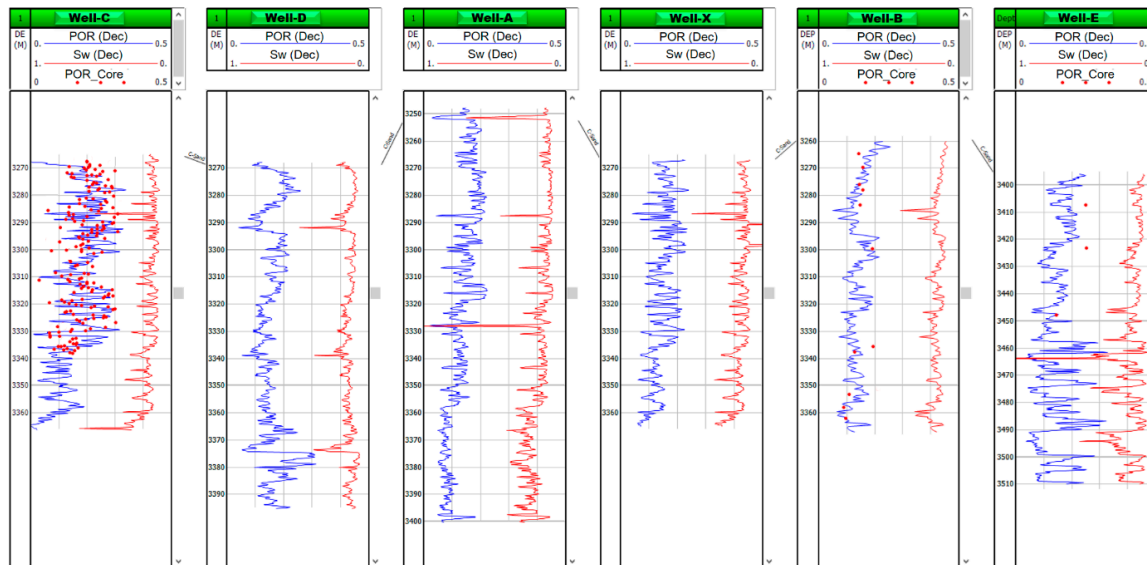


Figure 4. Estimated petrophysical properties of reservoir C-sand interval in the study wells; estimated values are shown in continuous lines while laboratory measurement results are indicated with red dots.

3.1.1. Petrographic and SEM Image Analysis

To distinguish bulk mineralogy from reactive mineralogy as a function of pore size, the study of the thin sections and SEM images was conducted in the laboratory. It was found that quartz arenite is dominant in lower Goru Formation that shows advanced diagenetic alteration throughout the type section (Figure 5a–d). The sandstones texturally change from medium to coarse-grained and fair to well-sorted with different frameworks of compaction and cementation. The grain-size varies from less than 0.06 to greater than 2 mm.

A thin section from Well-C shows diagenetic features such as compaction and cementation by high amounts of Fe-chlorite, Fe-dolomite, and calcite cementation (Figure 5a). The prevalent cemented framework is quartz (Q), carbonate, and chlorite (Chlr), commonly having a patchy distribution. The dissolution of feldspar grains (Fsp) and volcanic rock fragments (VRF) results in secondary porosity. In the thin sections, good to excellent porosity can be observed which is in accordance with the log porosity. Note that at certain locations, the components of cementation are fully dissolved except for the chlorite rims covering the remaining grains. The chlorite is present in the form of pore-lining cement covering all detrital grains (Figure 5c).

The diagenetic features in Well-D are characterized by quartz (Q) cementation as pore filling with idiomorphic quartz outgrowths (Figure 5b). The overgrowths of quartz (Qo) appear along chlorite rims coated with detrital quartz grains. It was developed where chlorite rims covered detrital quartz grains as shown in Figure 5d. The thin section shows good porosity with interconnected pores that help to enhance the reservoir characteristics. Also, secondary porosity can be observed due to dissolution and fracturing. The diagenetic features show that the Goru formation is distinguished by a potential reservoir with good porosity ranges.

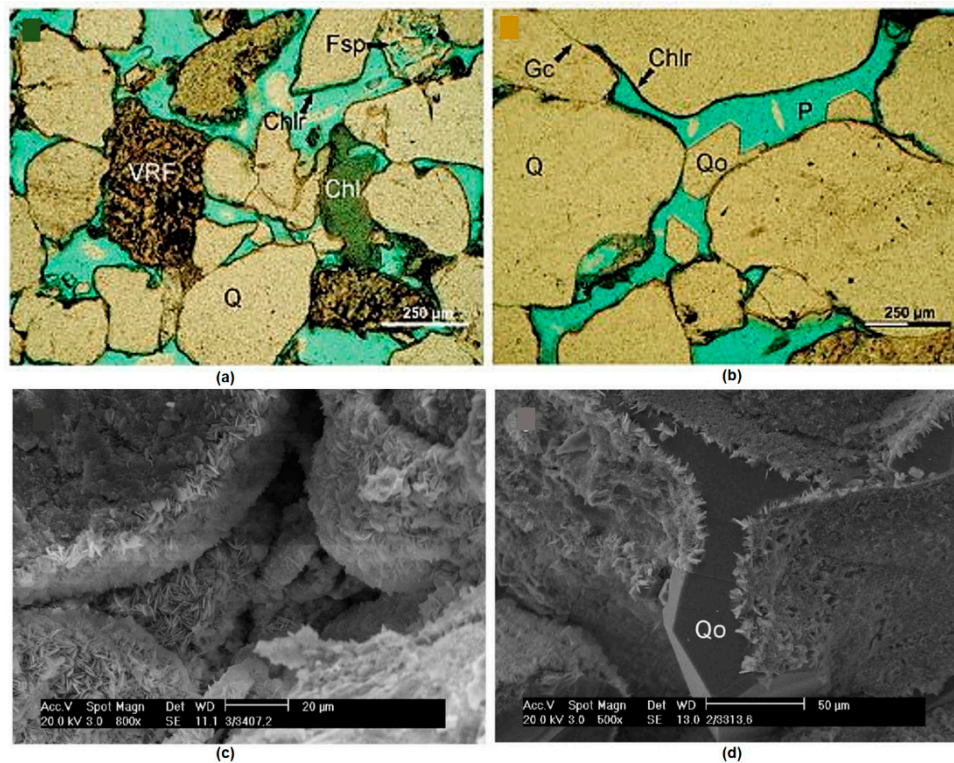


Figure 5. Thin sections (a,b) and SEM images (c,d) of the C-sand interval demonstrate the depositional and diagenetic characteristics, where Chl = chlorite, Chlr = chlorite rim, Q = quartz, Fsp = dissolving of feldspar grains, VRF = alteration of volcanic rock fragments, Qo = Idiomorphic quartz outgrowths filling partially the pores after Chlr, Gc = Grain contact. P = porosity is 15.3 to 22% in wells C and D [24].

3.1.2. NMR Investigation of the Cores and SEM Image Analysis

Nuclear magnetic resonance (NMR) is one of the most reliable tools for characterizing the porous media in the oil and gas industry nowadays [25,26]. In the present study, to better understand the pore size distribution within the C-sand interval, we measured NMR relaxation phenomenon of fully water-saturated cores. The samples were saturated with fresh water for 48 h and the measurements of relaxation phenomenon were conducted with an inter-echo spacing time (TE) of 0.2 ms and a waiting time for polarization (TW) of 6000 ms. The number of relaxation peaks was set at 10,000 whereas the number of scans was set to 64. Figure 6 shows four relaxation curves within the samples which are selected as the representative of the major types of pore size distributions observed within all the studied cores.

As generally known, three main peaks usually appear on an NMR T_2 distribution curve. These three peaks correspond to three different pore sizes respectively being micropores, macropores, and fractures (both micro and macro) which respectively appear from shorter to longer T_2 times on the horizontal time axis. Therefore, samples S1 (Figure 6a), and S4 (Figure 6d) show the dominance of the fractures in the reservoir area while samples S2 (Figure 6b) and sample S3 (Figure 6c) represents the high number of macropores. These observations coupled with the non-dominance of micropores in the samples verify the high porosity of the subject area as observed in the obtained modeling results of the present study.

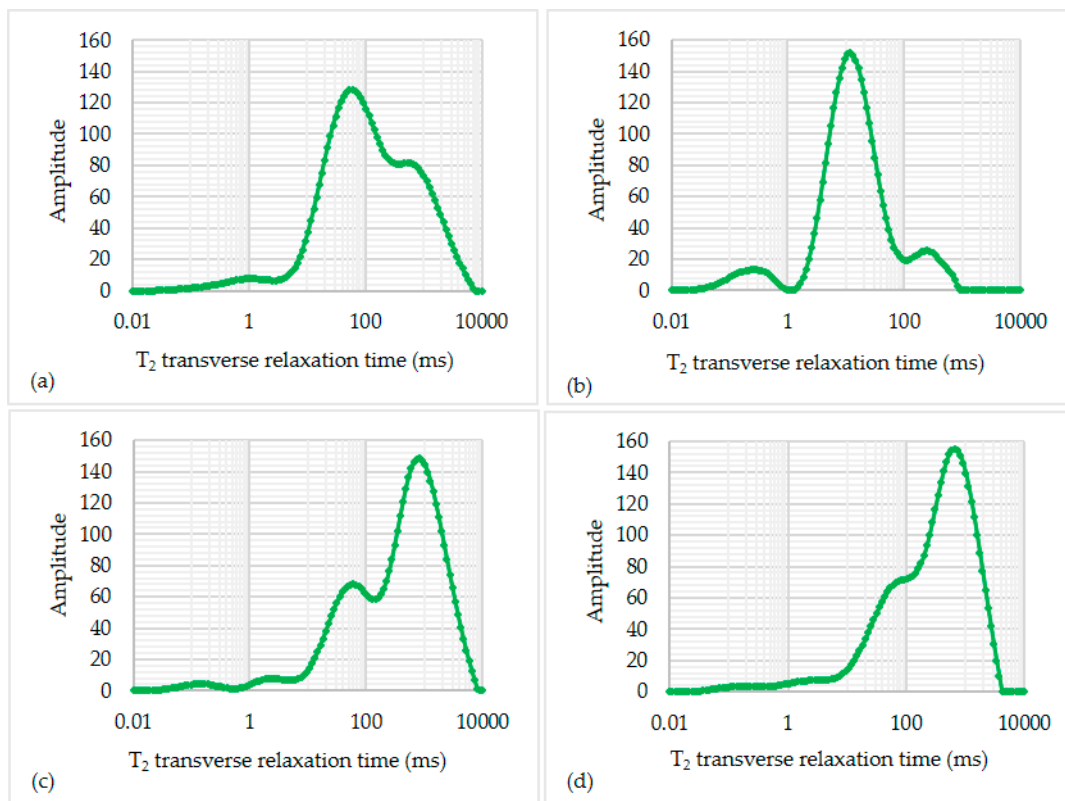


Figure 6. Typical T_2 relaxation curves observed for the core sample from the study area show various distributions of micro to macropores which result in the complex nature of the reservoir interval of the Sawan gas field, (a) sample S1, (b) sample S2, (c) sample S3, and (d) sample S4.

3.1.3. Facies Analysis and Modeling

For reservoir modeling, the initial grid structure was performed with 71,760 cells and $92 \times 78 \times 10$ dimensions. However, throughout the upscaling of the well logs, it was impossible to pick the thin shale layers and channel sandstone in the reservoir. Also, the reservoir layering with high producible hydrocarbon was not taken into consideration by 3D modeling. Since the geological features that were smaller than the grid layering were ignored when upscaling well logs, the upscaled reservoir model was not able to estimate the low-resolution lithological features from well log analysis. To resolve this issue and improve the resolution and predictive capability, a high-resolution model with 72,649,401 cells and $920 \times 780 \times 100$ dimension was developed to identify the thin shale layering and channel sandstone within the reservoir interval. The structural grid models with low and high-resolution grid cells are shown in Figure 7. It is shown that the high-resolution grid structure with sufficient layering and grid cells improved the capability of the model to recognize the facies and petrophysical properties from well logs.

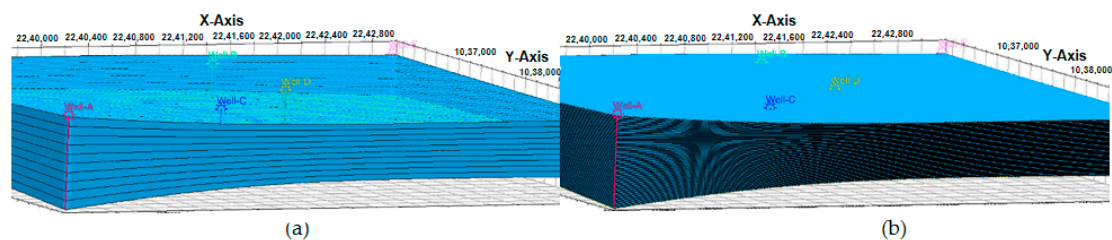


Figure 7. Structural grid of the studied reservoir; (a) Low-resolution grid cells (71,760 cells), (b) High-resolution grid cells (72,649,401 cells).

Figure 8 shows the well correlation for facies distribution with low and high-resolution grid cells in C-sand interval using the GR log response. It is worth noting that the high-resolution grid structure successfully captured the thin layers of shale and shaly sands. From the figure, we observe that the lower part of the reservoir interval is more heterogeneous because the shale and shaly sand are abundant. In the upper part of the reservoir interval, sandstone is dominant in Well-C, D, and E. However, several thin shale and shaly sand layers can be observed in the reservoir. Note that the GR curve in Well-B shows distinct behavior as compared to Well-A, C, D, and E and demonstrates shaly sandstone and shale as dominant lithofacies in the entire zone.

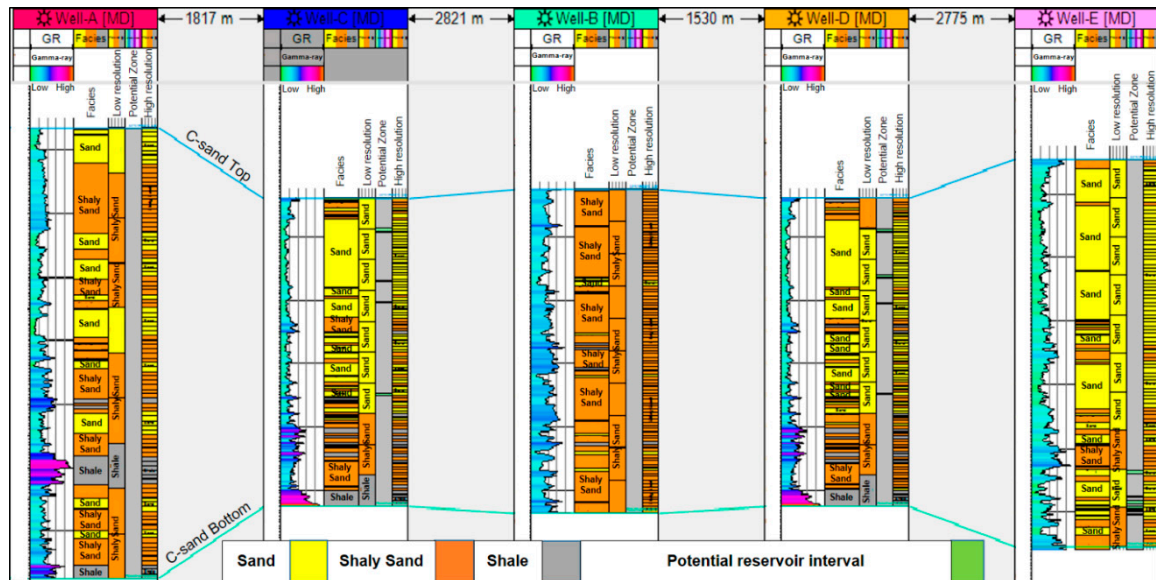


Figure 8. Comparison of facies analysis; Track B: Gamma-ray log, Track C: Facies analysis from well logs, Track D: Facies analysis from low-resolution up-scaling, Track E: Facies analysis from high-resolution up-scaling, and Track F: Potential reservoir zones.

In the reservoir interval, the good quality potential zones were marked on the basis of better petrophysical properties. The pay zone cutoff used in the reservoir interval was as follows; i.e., general_discrete (suggested perforation interval) = If (Facies = Sand, where $SW < 30$, $PHI_D > 0.3$, $PHI_{EFF} > 0.2$, and $PERM > 5$ mD, suggested perforation interval, undefined). The potential zones are shown in track E of Figure 8.

The spatial distribution of facies over the entire Sawan gas field was performed by the GIS algorithm to spread discrete data spatially. The result of the spatial distribution of facies is shown in Figure 9. Note that the upper part of the reservoir in Well-A, C, and D is composed of sandstone lithofacies but it changes into to shaly sandstone and finally shale lithofacies at the bottom part of the reservoir interval. The mid-section of the reservoir is mainly composed of sandstone but converted into shale heterogeneities laterally towards south. The 3D view of the spatial distribution of facies shows that entire type section is mainly composed of sandstone, shaly sandstone, and shale lithofacies (Figure 9a). Meanwhile, high shale content present at the bottom of the reservoir increasing towards SE (Figure 9b). The average value of each lithology is identified as; sandstone 34.2%, shaly sandstone 44.6% and shale 21.2%. The reliability of the GIS algorithm-based model was accessed by studying the level of matching between different facies trends in the well log analysis, up-scaled well logs, and modeled facies. It is to be noted that the spatial distribution of facies modeling shows good matching with AI map extracted from 3D seismic inversion techniques, i.e., AI varies enormously depending on the variations of lithology in each zone.

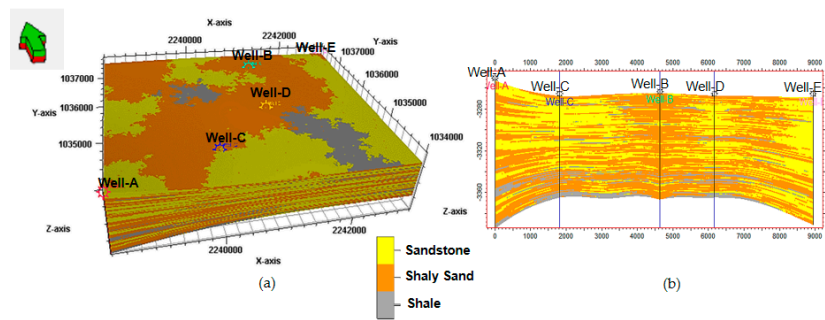


Figure 9. The petrophysical modeling and inversion of facies (a) 3D facies model, (b) cross-sectional view of the 3D facies model.

3.2. Reservoir Characterization from Seismic Data

The first step of inverting seismic reflection data into petrophysical parameters is to calibrate the well logs and seismic data for the construction of a synthetic seismogram. To compute a synthetic seismogram, the sonic and bulk density logs along with check shot data (time-depth relation or TDR) of Well-C, as well as 3D seismic data, were loaded into the software. The aligned sonic velocity (V_P) and RHOB log curves were refined and multiplied to obtain acoustic impedance (AI) as given in Equation (10). From AI, the reflection coefficient (RC) for each reflecting interface was computed using Equation (11). The software enabled the use of either a Ricker wavelet or a wavelet from the original seismic line for the convolution of reflection time series, in order to generate a synthetic trace. Based on iterative trials that ultimately yielded the best comparison between the seismic and synthetic seismogram, a Ricker wavelet with fixed parameters (128 ms sample lengths, two-ms sample rate, and 25 Hz frequency) was selected to generate the synthetic trace. The wavelet was extracted from the seismic dataset within a prescribed time window, i.e., 2140 ms to 2280 ms, including the traces from inline and cross-line. A minor amount of time-stretching and squeezing was applied to align the seismic and synthetic seismogram reflectors. The final position of the reflectors closely matched the depths of the respective horizons (e.g., C-sand top and C-sand bottom). Figure 10 shows a post-stack seismic inversion analysis plot of well to seismic tie along with the computed extracted wavelet, reflectivity series, and the synthetic seismogram for Xline 932.

$$AI = \rho \times V \tag{10}$$

$$RC = \frac{(A.I)_{layer-1} - (A.I)_{layer-2}}{(A.I)_{layer-1} + (A.I)_{layer-2}} \tag{11}$$

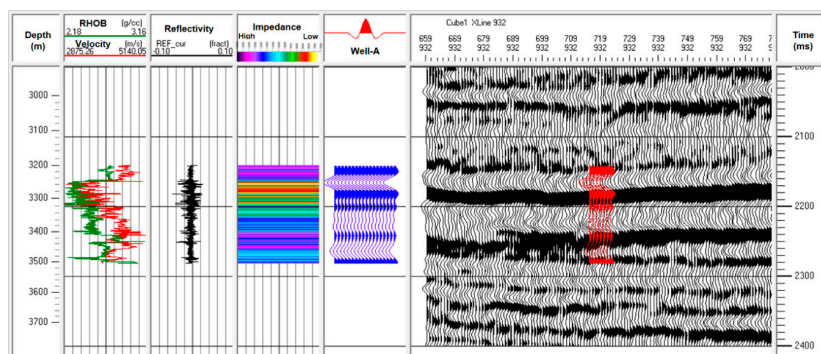


Figure 10. Synthetic seismogram for Well-C, showing (left to right): TVD (true vertical depth) in meters, sonic transit time ($\mu\text{s}/\text{ft}$) and bulk density from logs (g/cm^3), RC (reflection coefficient), synthetic seismogram, traces from a portion of seismic Xline 932, and TWT (two-way time in ms).

In this case, the wavelet properties and spectrum used for the computation of synthetic seismogram, are shown in Figure 11.

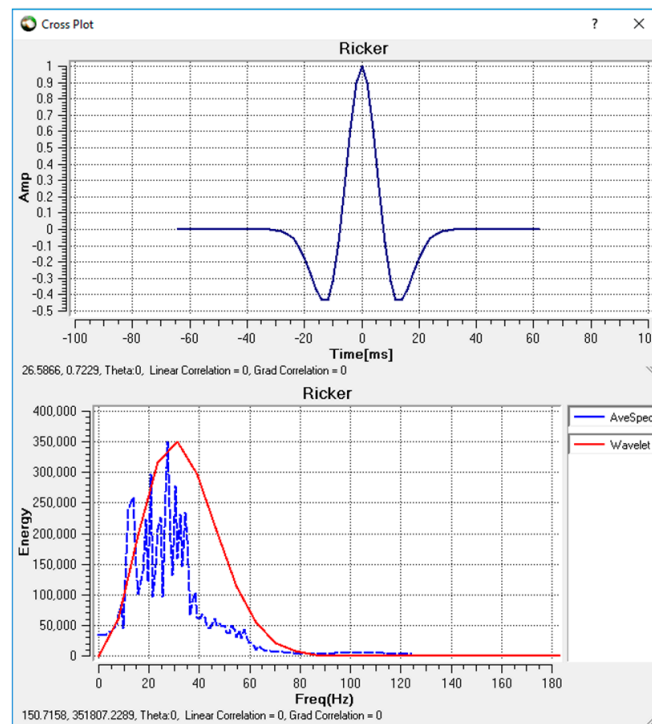


Figure 11. The plots of the extracted wavelet (Time-Amplitude, Frequency-Power, Frequency-Phase) for correlation between seismic and well log in time and frequency at 2000–2300 ms.

3.2.1. Seismic Inversion

Figure 12 indicates the result of SVM inversion applied to the Xline 932 of the 3D seismic cube. It is shown that the SVM inversion was successful in capturing the spatial variations of AI contrast. The intended zone of interest (C-sand interval) lies from 2140 to 2280 ms, and the AI varies from 7000 to 13,000 $(\text{g/cc}) \times (\text{m/s})$ in the reservoir interval. Note that the variation of AI correlates very closely with major lithological changes between adjacent rock layers. The time interval of 2160 to 2185 ms has low AI (7500–9500 $(\text{m/s}) \times (\text{g/cc})$), reflecting then probably the presence of a good quality reservoir (hydrocarbon-bearing zone) at this particular level (shown with arrows). The overlying blue-pink layers above the low impedance layer (2160 ms) show impedance values between 10,500 to 14,000 $(\text{m/s}) \times (\text{g/cc})$, which is assumed to be a seal unit above the reservoir interval. The pattern of low and high impedance layers are due to the alternate sand-shale and channel sandstone present at this location (shown with arrows). It is important to note that the thin shale and shaly sand layers existed below and above the sandstone lithofacies (Figure 9) but SVM inversion observed the changes and successfully captured the AI contrast (Figure 12, shown with arrow). Although complex and nonlinear relationship exists between the thinly layered media and seismic waveforms, SVM established nonlinear projection relationship to capture the thinly layered media from the seismic waveform. In contrast, the inverted AI from model-based or other traditional algorithms applied previously in the same dataset have not been good enough to capture the small lithological variations [18,19]. What is more, overall lateral and vertical variations in the resolution of AI estimated from traditional inversion algorithms was poor and resulted in discontinuity of seismic event.

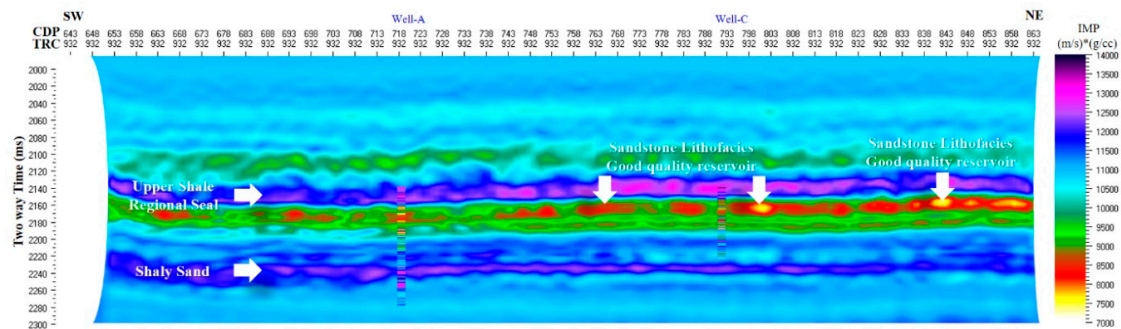


Figure 12. The inverted AI for Xline 932 using SVM seismic inversion. The impedance log of well-A, C, and D are not in good match with the inverted impedance surface.

The comparison of the original AI logs with those computed from SVM inversion analysis for Xline 932 is shown in Figure 13 which represents a reasonably good agreement. The overall correlation coefficient between the original and the computed values were equal to 0.87, 0.71, and 0.93 in Well-A, C, and D respectively. This high correlation coefficient indicates the reliability and accuracy of the SVM inversion approach.

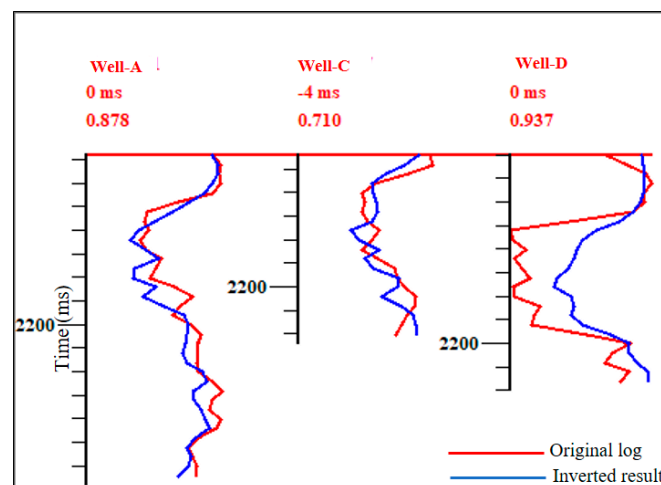


Figure 13. Comparison of original logs (blue) and SVM-inverted results (red) at Well-A, Well-C, and Well-D by SVM inversion method.

3.2.2. Reservoir Character (Porosity) Estimation

In this section, we discuss the reservoir character estimation from post-stack seismic data. The AI-derived from SVM inversion is linked with seismic attributes used for reservoir modeling and characterization. Hampson et al. [10] defined seismic attribute as an inversion of seismic trace into an important petrophysical property. The significance of seismic attributes for reservoir character estimation has been stated by various researchers [27–30].

In the present study, a logical correlation (petro-elastic) between seismic attributes and petrophysical properties was established to transform the porosity and saturation variations from 3D post-stack seismic data. Figure 14 shows the cross-plot of porosity versus AI with hydrocarbon saturation taken as a third parameter. From the figure, it is shown that while decreasing AI, the porosity and hydrocarbon saturation increase. A linear relationship between porosity and hydrocarbon saturation versus AI can be observed with a negative slope. Ali et al. [18] reported that the relationship between AI and estimated porosity is always linear in nature. Therefore, linear regression analysis was used for this study. The regression equations obtained from the cross-plot was used to transform the AI inversion into reservoir parameters.

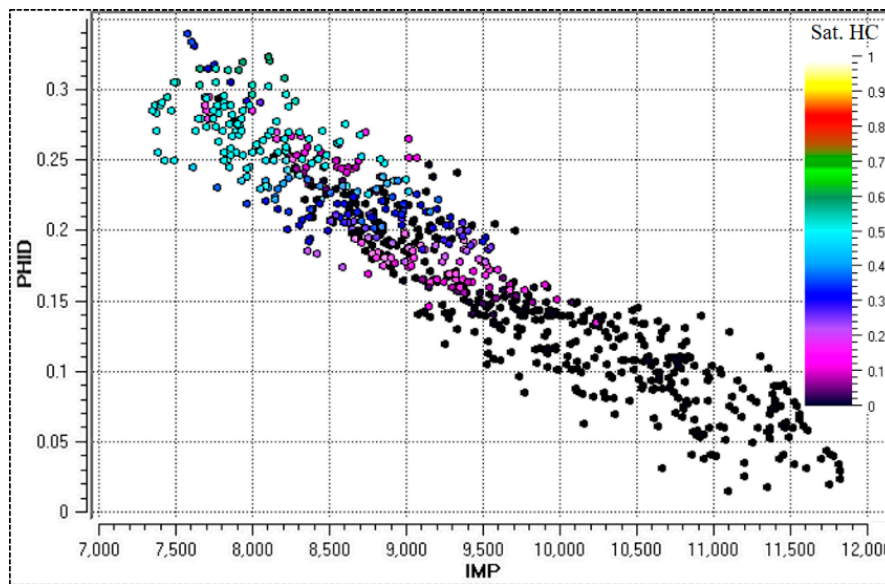


Figure 14. A cross-plot of acoustic impedance (AI) and porosity with a color bar representing hydrocarbon saturation values (Sat. HC).

In Figure 15, the inverted impedance surface in the reservoir interval is linked into a recursive inversion solution for porosity. The seismic cube was scaled for porosity and then was calibrated by Well-A, C, and D. A favorable distribution of porosity can be observed along with low impedance values of the Well-A, C, and D at the intended zone of interest (2160 to 2180 ms). The porosity varied from a minimum of 10% (Well-A) to a maximum of 30% (Well-C and D), in SW to NE direction, with an average of around 18%. Noted that below 2200 ms, we could observe relatively high porosity with medium to a high impedance that corresponds to shaly sand with subordinate sand and shale layers (Figure 9).

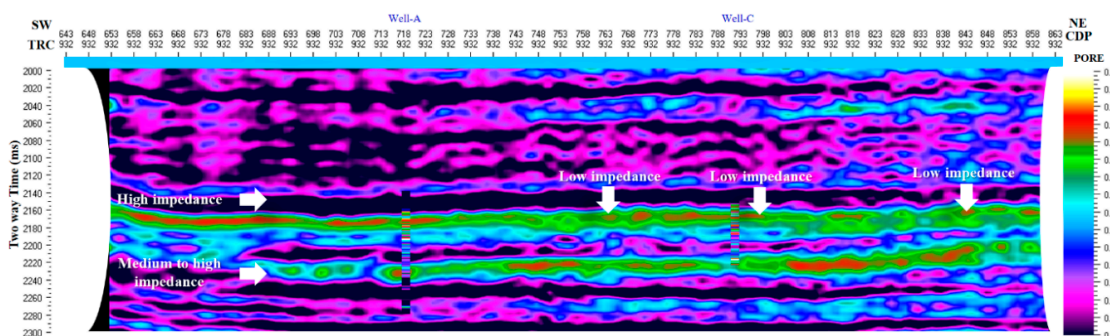


Figure 15. The seismic inversion map of effective porosity for C-sand interval (2140 ms to 2280 ms).

The 3D visualization maps for both AI and effective porosity clearly indicated high-quality reservoir zones around the Well-A, B, C, and D, laterally and vertically in the entire region (Figure 16a,b). It can be observed that the porosity varies from a maximum of 25% (red color) to minimum of 5% (pink color) along with the range of AI varying from 6000 to 13,000 (g/cc) × (m/s). Herein, it is important to point out that low AI layers are consistent with high porosity values over the entire field as compared to previous studies in the region [18]. However, in the middle of the reservoir interval (vertically), high porosity layer is visible but the values of AI is also high at this particular location. It is due to the presence of shaly sand with subordinate sand and shale layers.

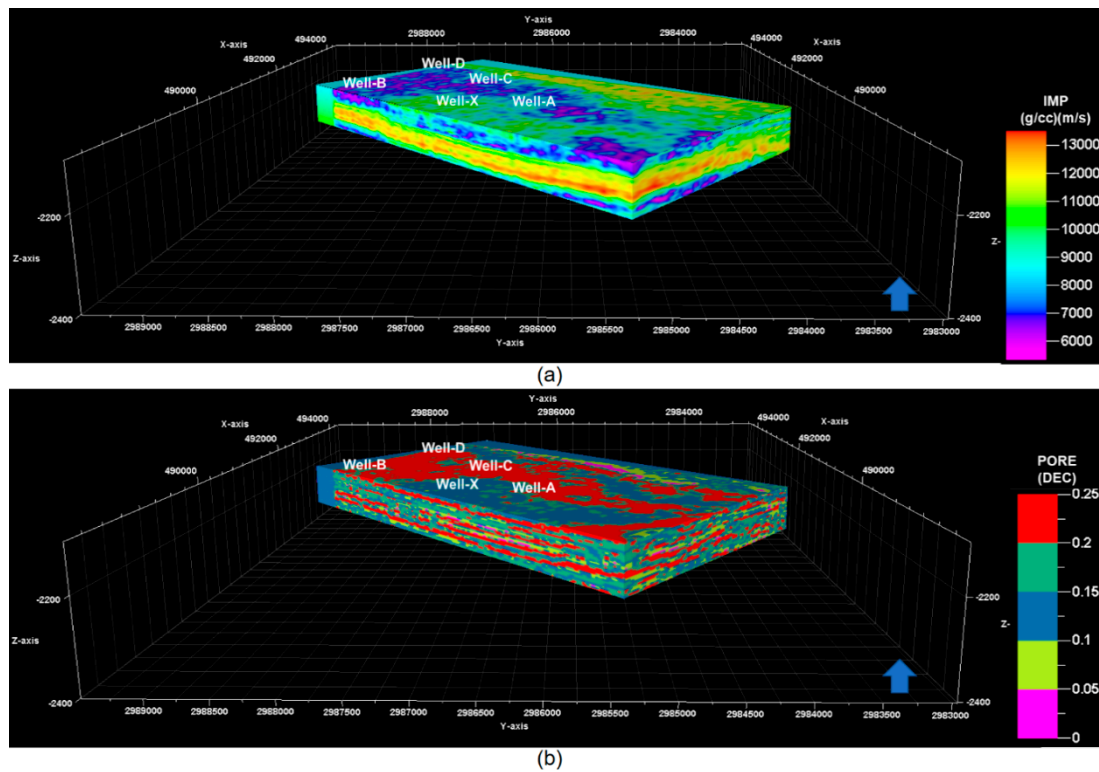


Figure 16. (a) 3D AI model, (b) seismic inversion of 3D effective porosity models within a specified time window (2160 to 2280 ms) covering target horizons.

3.2.3. Integrated Petrophysical Data Interpretation

The results of the effective porosity estimation from petrophysical modeling are shown in Figure 17. From the figure, it is shown that the area around the Well-A shows very good effective porosity, i.e., more than 25% but gradually decrease towards SW at Well-B reaching to about 10%. It should be noted that sandstone lithofacies are dominant in the upper part of the reservoir interval which results in high effective porosity. In Figure 17 which illustrates the first, second, and third cross-sectional analysis, the effective porosity is increasing along the SW to NE of the Well-A, C, and D. It is important to note that high range of effective porosity is consistent with sandstone lithofacies in the vicinity of the Well-A, C and D. However, the distribution of the shale and shaly sand in the reservoir are main factors controlling the reservoir potential in the study area.

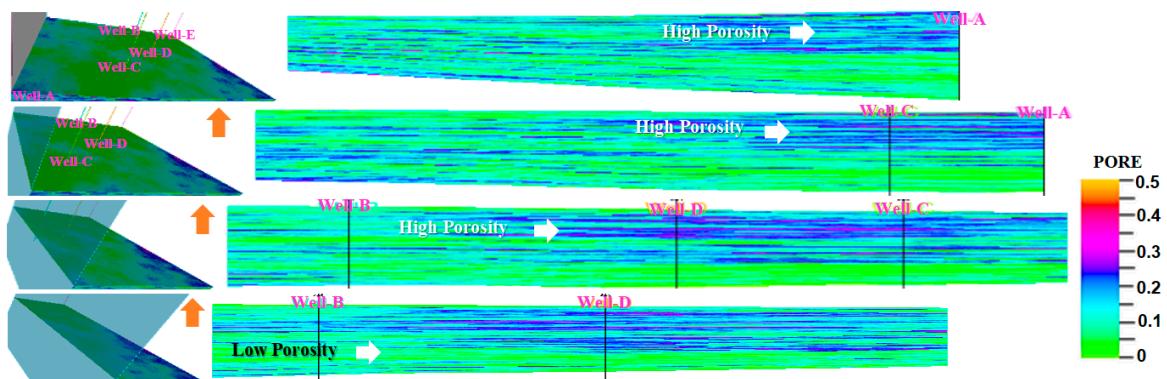


Figure 17. The cross-sectional analysis of 3D effective porosity model by well log simulation of C-sand interval.

To get a more reliable insight into the spatial variability of effective porosity in the reservoir interval, the time slices at the interval of 20 ms are generated using SVM inversion method. In Figure 18a–c, the Z-1, Z-2, and Z-3 show high porosity regions around the wells that significantly improve our confidence to delineate a high-quality reservoir. Also, the laboratory-measured porosity data in Well-C and Well-D and cross-sectional analysis by well log simulation are closely matched with the inverted results, i.e., the upper zone (3270 to 3330 m) is highly porous, as displayed in Figure 4. Alternatively, the Z-4 indicates relatively low to high porosity regions (Figure 18d) and is characterized by medium to high impedance that corresponds to sandstone with subordinate shale (Figure 12). The laboratory-measured porosity data in Well-C and Well-D (Figure 4) and cross-sectional analysis (Figure 17) also show low to high porosity range at this particular level (3330 to 3360 m).

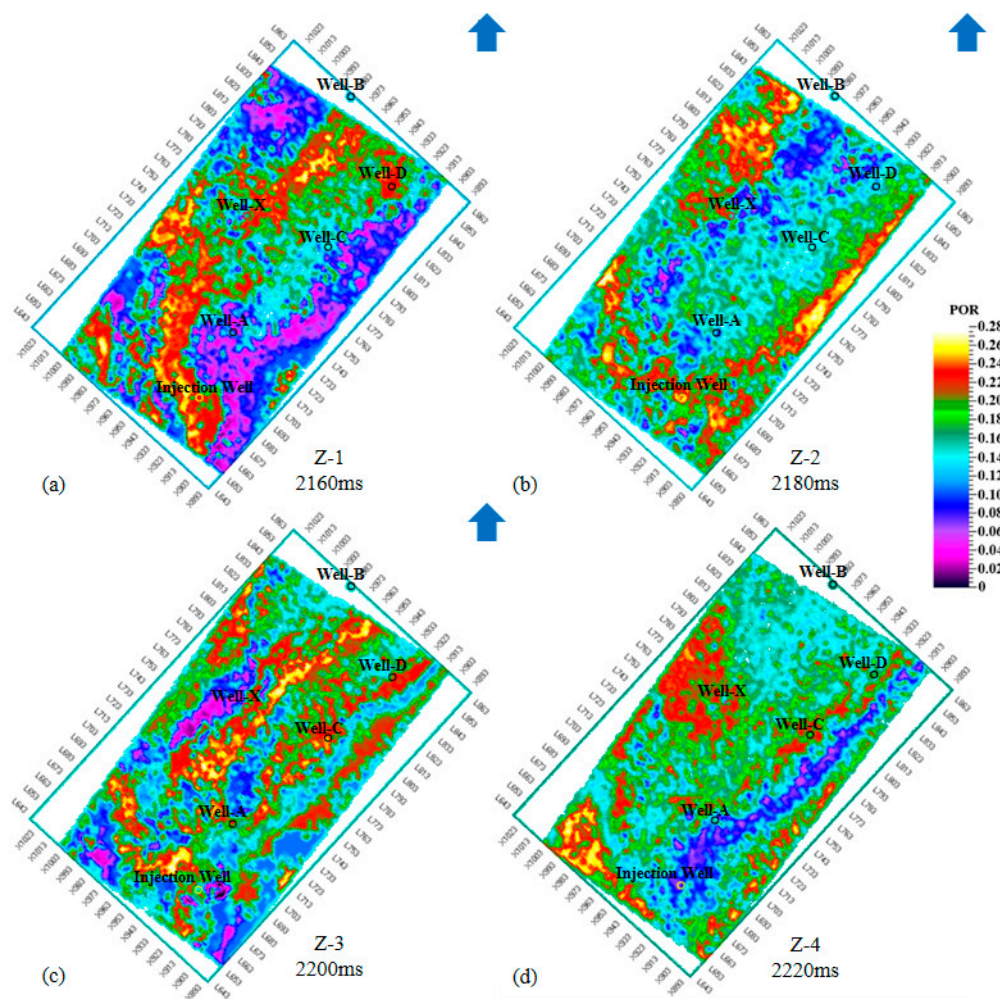


Figure 18. The time slice of porosity at various interval, (a) 2160 ms, (b) 2180 ms, (c) 2200 ms, and (d) 2220 ms.

4. Prediction of Reservoir Quality

For reservoir characterization, the porosity, permeability, and hydrocarbon saturation are inherent properties, but the quantitative estimation of these properties is as difficult as their importance. More problems could arise in the evaluation of petrophysical parameters when intercalated shale (dispersed shale) is trapped in the reservoir interval [31]. Traditionally, porosity and permeability are determined by wireline log data, numerical models, and core-based laboratory procedures. The well data and laboratory measurements provide the best and more accurate vertical resolution for the estimation of porosity and permeability but this remains a local estimation, i.e., it is limited to only certain locations

(near to wellbore). Thus, it is uncertain to estimate the spatial distribution of porosity and permeability in a whole region just from well logs data. The integration of petrophysical modeling with seismic inversion results presents a reliable and widely accepted approach to achieve the right estimation of the spatial distribution of the most crucial reservoir properties.

To develop a reservoir quality prediction of C-sand interval, the inverted profiles of AI, porosity, and hydrocarbon saturation (Sat. HC) using the SVM technique were integrated to define the high-quality reservoir regions. In Figure 19a,b, the high-quality regions are drawn with a polygon to track the reservoir extension in the Sawan gas field. It is shown that the region around NE of the Well-A has high saturation, i.e., more than 80% (Figure 19b). Also the region lying between Well-A and Well-C shows good properties for oil and gas production, i.e., Sat. HC is around 80% and porosity is 14–24% (Figure 18c). Note that the production data of the Well-A and Well-C indicate maximum production in these wells (Table 1). The regions around Well-D and injection well (NW) also reveal good reservoir properties (porosity > 24% and Sat. HC > 80%). The time slice of AI shows lower values along with high saturation regions (outlined with a polygon) (Figure 19a). In general, Sat. HC varies in the region from 20% (pink color) to 80% (red color). The majority of the studied area (66%) proved to be of good reservoir quality with significantly high porosity and Sat. HC coupled with lower AI. More importantly, high-quality regions are mainly composed of sand and shaly sand lithofacies (Figures 8 and 9).

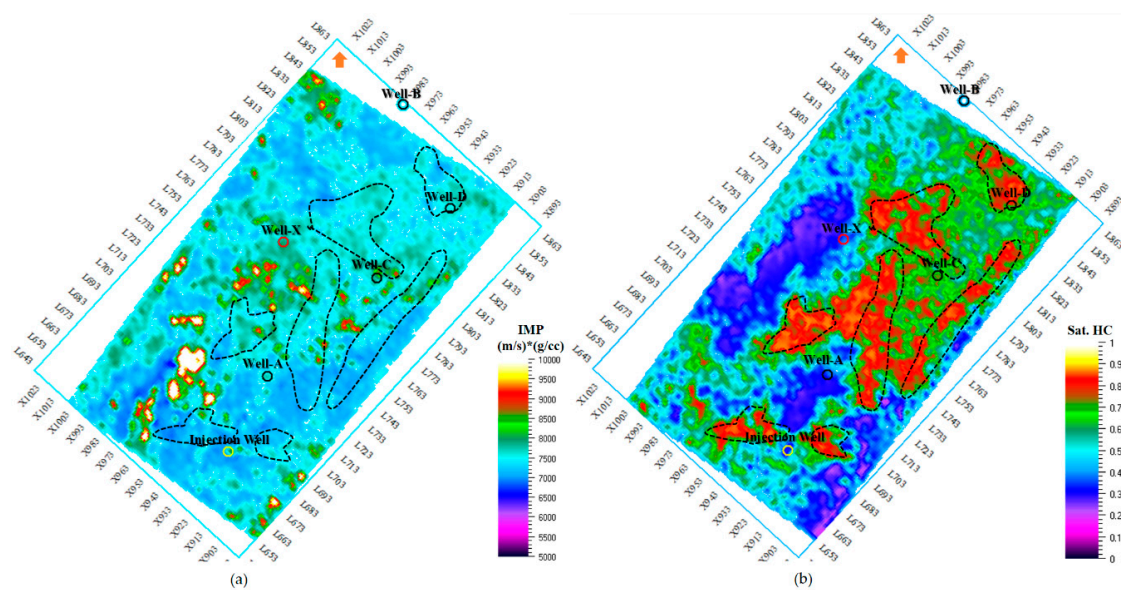


Figure 19. The time slices of (a) AI, (b) hydrocarbon saturation (Sat. HC) at $Z = 2200$, demonstrating the prospects within the target reservoir interval.

Table 1. Production data from the study wells [2].

Well ID	Production (MMscf)
Well-A	12.779
Well-C	24.428
Well-D	13.760
Well-X	04.703

To better explain and differentiate the Sat. HC in the reservoir interval, the 2D maps of two attributes namely “amplitude above average” and “low-frequency attenuation gradient” at $Z = 2200$ ms were extracted from 3D seismic data (Figure 20). The high amplitude and low-frequency values are the indications of gas reservoir [32]. In Figure 20, the two attribute maps exhibit good correspondence along with high Sat. HC regions and clearly demonstrate the gas saturation at this particular location.

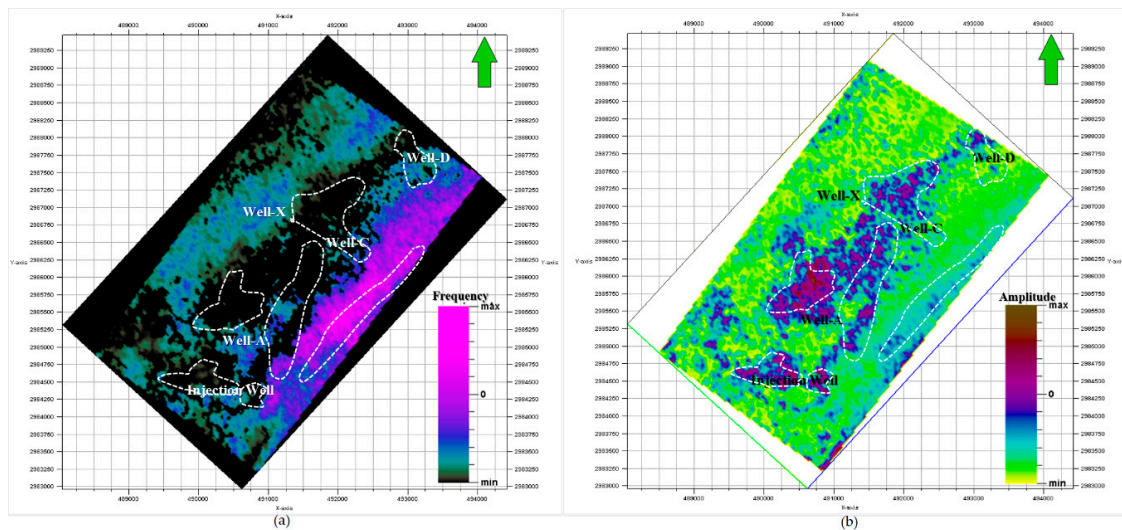


Figure 20. 3D Seismic attributes map, (a) low-frequency attenuation gradient, (b) amplitude above average at $Z = 2200$ ms, demonstrating the high amplitude (maroon) is being consistent with low-frequency (black).

5. Conclusions

This study presents a novel approach that aims to predict the quality of a petroleum reservoir from the analysis of well logs, core data, and 3D seismic data. ML-based inversion algorithm was selected to predict the spatial variations of AI, porosity, and saturation through training and validation of suitable seismic attributes and measured properties in well logs. In supervised mode, the SVM inversion algorithm performed efficiently in identifying and mapping individual reservoir properties to delineate and quantify fluid-rich zones. The calibration of the detailed spatial variations from post-stack seismic inversion using SVM and wireline logs simulation using SGS and GIS indicated an appropriate agreement, i.e., variations in AI is related to the variations in reservoir facies and parameters. Since complex and nonlinear relationship exists between the thinly layered media and seismic waveforms, SVM established nonlinear projection relationship and captured the thin layers and channel sandstone from the seismic reflection data. Thus, SVM is more reliable than the traditional inversion algorithm to discriminate lateral and vertical facies heterogeneity. Therefore, this new approach can be used as a proxy for inverting the seismic reflection data into volume or cube of the reservoir property in complex reservoir.

The time slices of the inverted porosity and hydrocarbon saturation show that the area around NE of the Well-A and Well-C have high porosity ($\sim 26\%$) with hydrocarbon saturation more than 80%. Moreover, the production data of the Well-A and Well-C indicated gas production from 12.779 MMscf to 24.428 MMscf respectively. Meanwhile, the attributes map of the “amplitude above average” and “low-frequency attenuation gradient” differentiated the hydrocarbons into a gas saturated reservoir.

Author Contributions: Conceptualization, Z.Q.; Formal analysis, Q.D. and Q.Y.; Investigation, Q.Y.; Methodology, Z.Q.; Supervision, Q.D.; Validation, N.G.; Writing—original draft, Z.Q. and Q.Y.; Writing—review & editing, N.G. All authors have read and agreed to the published version of the manuscript.

Funding: This research received no external funding.

Acknowledgments: This work is supported by National Science Foundation of China (41930429 and 41774139), the research project of the China National Petroleum Corporation under grant number 2019A-33, China National ‘111’ Foreign Experts Introduction Plan for Tight Oil & Gas Geology and Exploration, and Deep-Ultradeep Oil & Gas Geophysical Exploration. We are grateful to Beijing Rock Star Petroleum Technology Co., LTD for providing software support and lab facilities.

Conflicts of Interest: The authors declare no conflict of interest.

Acronyms

AI	Acoustic Impedance
CAL	Caliper
DTP	P-wave sonic
DTS	S-wave sonic
GIS	Gaussian Indicator Simulation
GR	Gamma-Ray
LLD	Deep Resistivity
ML	Machine Learning
NPHI	Neutron Porosity
NMR	Nuclear Magnetic Resonance
RBF	Radial Basis Function
RHOB	Bulk Density
SVM	Support Vector Machine
SV	Support Vectors
SGS	Sequential Gaussian Simulation
SP	Spontaneous Potential
Sat. HC	Hydrocarbon Saturation
TCF	Trillion Cubic Feet
MMscf	Millions Cubic Feet
Ms	milli-second

References

1. Abdulrauf, R.A.; Babalola, L.; Hussaini, S.R.; Alqubalee, A.; Babu, R.S. Insight into the Pore Characteristics of a Saudi Arabian Tight Gas Sand Reservoir. *Energies* **2019**, *12*, 4302. [[CrossRef](#)]
2. Ashraf, U.; Zhua, P.; Yasin, Q.; Anees, A. Classification of reservoir facies using well log and 3D seismic attributes for prospect evaluation and field development: A case study of Sawan gas field, Pakistan. *J. Pet. Sci. Eng.* **2019**, *175*, 338–351. [[CrossRef](#)]
3. Yasin, Q.; Du, Q.; Sohail, G.M.; Ismail, A. Fracturing Index-based Brittleness Prediction from Geophysical Logging Data: Application to Longmaxi Shale. *Geomech. Geophys. Geo Energy Geo Resour.* **2018**, *4*, 301–325. [[CrossRef](#)]
4. Liu, J.; Ning, J.R.; Liu, X.W.; Liu, C.Y.; Chen, T.S. An Improved Scheme of Frequency-Dependent AVO Inversion Method and Its Application for Tight Gas Reservoirs. *Geofluids* **2019**, *2019*, 3525818. [[CrossRef](#)]
5. Yasin, Q.; Du, Q.; Yuan, G.; Ismail, A. Application of hydraulic flow unit in pore size classification. *SEG Tech. Program Expand. Abstr.* **2017**, 3872–3876. [[CrossRef](#)]
6. Walls, J.D.; Taner, M.T.; Taylor, G.; Smith, M.; Carr, M.; Derzhi, N.; Drummond, J.; McGuire, D.; Morris, S.; Bregar, J.; et al. Seismic reservoir characterization of a U.S. midcontinent fluvial system using rock physics, poststack seismic attributes, and neural networks. *Lead. Edge* **2002**, *21*, 428–436. [[CrossRef](#)]
7. Pramanik, A.G.; Singh, V.; Vig, R.; Srivastava, K.; Tiwary, D.N. Estimation of effective porosity using geostatistics and multi-attribute transforms: A case study. *Geophysics* **2004**, *69*, 352–372. [[CrossRef](#)]
8. Calderon, J.E. Porosity and lithologic estimation using rock physics and multi-attribute transforms in Balcon Field, Colombia. *Lead. Edge* **2007**, *26*, 142–150. [[CrossRef](#)]
9. Demuth, H.; Beale, M.; Hagan, M. *Neural Network Toolbox™ 6. User's Guide*; The MathWorks TM: Natick, MA, USA, 2008; p. 907.
10. Hampson, B.; Schuelke, J.; Quirein, J. Use of multi-attribute transforms to predict log properties from seismic data. *Geophysics* **2001**, *66*, 3–46. [[CrossRef](#)]
11. Golsanami, N.; Sun, J.M.; Liu, Y.; Yan, W.C.; Chen, L.J.; Jiang, L.S.; Dong, H.M.; Zong, C.L.; Wang, H.Q. Distinguishing fractures from matrix pores based on the practical application of rock physics inversion and NMR data: A case study from an unconventional coal reservoir in China. *J. Nat. Gas Sci. Eng.* **2019**, *65*, 145–167. [[CrossRef](#)]
12. Russell, B.H. *Introduction to Seismic Inversion Methods*; Society of Exploration Geophysicists: Tulsa, OK, USA, 1988; p. 86.

13. Yasin, Q.; Du, Q.; Ismail, A. A new integrated workflow for improving permeability estimation in a highly heterogeneous reservoir of Sawan Gas Field from well logs data. *Geomech. Geophys. Geo Energy Geo Resour.* **2019**, *5*, 121–142. [CrossRef]
14. Kelkar, M.; Perez, G.; Chopra, A. *Applied Geostatistics for Reservoir Characterization*; Society of Petroleum Engineers: Richardson, TX, USA, 2002.
15. Droz, L.; Bellaiche, G. Seismic Facies and Geologic Evolution of the Central Portion of the Indus Fan. In *Seismic Facies and Sedimentary Processes of Submarine Fans and Turbidite Systems*; Springer: New York, NY, USA, 1991; pp. 383–402.
16. Du, Q.; Yasin, Q.; Ismail, A.; Sohail, M. Combining classification and regression for improving shear wave velocity estimation from well logs data. *J. Petroleum Sci. Eng.* **2019**, 182. [CrossRef]
17. Ahmad, N.; Fink, P.; Sturrock, S.; Mahmood, T.; Ibrahim, M. Sequence Stratigraphy as Predictive Tool in Lower Goru Fairway, Lower and Middle Indus Platform, Pakistan. Available online: http://www.searchanddiscovery.com/documents/2012/10404ahmad/ndx_ahmad.pdf?q=%2BauthorStrip%3Asturrock+-isMeetingAbstract%3Amtgabsyes (accessed on 10 October 2019).
18. Ali, A.; Alves, T.M.; Farhad, A.; Toqeer, M.; Hussain, M. Resource potential of gas reservoirs in South Pakistan and adjacent Indian subcontinent revealed by post-stack inversion techniques. *J. Nat. Gas Sci. Eng.* **2018**, *49*, 41–55. [CrossRef]
19. Asad, M.; Rahim, H.U. Porosity Distribution and Differentiation of Different Types of Fluids in Reservoir Of Sawan Gas Field, Lower Indus Basin, Pakistan. *Pak. J. Geol.* **2019**, *3*, 28–37.
20. Russell, B. Seismic Reservoir Characterization and Pre-Stack Inversion in Resource Shale Plays. Available online: http://www.searchanddiscovery.com/documents/2014/41467russell/ndx_russell.pdf (accessed on 10 October 2019).
21. Xu, C.C.; Misra, S.; Srinivasan, P.; Ma, S.X. When Petrophysics Meets Big Data: What Can Machine Do. Proceedings of SPE Middle East Oil and Gas Show and Conference, Manama, Bahrain, 18–21 March 2019. SPE-195068-MS.
22. Cortes, C.; Vladimir, V. Support-Vector Networks. *Mach. Learn.* **1995**, *20*, 273–297. [CrossRef]
23. Istrail, S.; Pavel, A.P. *Kernel Methods in Computational Biology*; MIT Press: Cambridge, MA, USA, 2004.
24. Berger, A.; Gier, S.; Krois, P. Porosity-preserving chlorite cements in shallow-marine volcanoclastic sandstones: Evidence from Cretaceous sandstones of the Sawan gas field, Pakistan. *AAPG Bull.* **2009**, *93*, 595–615. [CrossRef]
25. Yan, W.; Sun, J.; Golsanami, N.; Li, M.; Cui, L.; Dong, H.; Sun, Y. Evaluation of wettabilities and pores in tight oil reservoirs by a new experimental design. *Fuel* **2019**, *252*, 272–280. [CrossRef]
26. Golsanami, N.; Sun, J.; Zhang, Z. A review on the applications of the nuclear magnetic resonance (NMR) technology for investigating fractures. *J. Appl. Geophys.* **2016**, *133*, 30–38. [CrossRef]
27. Taner, M.T. Seismic attributes. *Can. Soc. Explor. Geophys. Rec.* **2001**, *26*, 46–56.
28. Tebo, J.M.; Hart, B.S. Use of volume-based 3-D seismic attribute analysis to characterize physical property distribution: A case study to delineate reservoir heterogeneity at the Appleton field, SW Alabama. *J. Sediment. Res.* **2005**, *75*, 723–735. [CrossRef]
29. Khoshdel, H.; Riahi, M.A. 3D porosity estimation using multi-attribute analysis methods in one of the Persian Gulf oil fields. In Proceedings of the SPE Europe/EAGE Annual Conference and Exhibition, London, UK, 11–14 June 2007.
30. Ogiesoba, O.C. Porosity prediction from seismic attributes of the Ordovician Trenton-Black River groups, Rochester field, southern Ontario. *Am. Assoc. Pet. Geol. Bull.* **2010**, *94*, 1673–1693. [CrossRef]
31. Sun, P.H.; Zhu, J.Y.; Zhao, B.K.; Zhang, X.X.; Cao, H.; Tian, M.J.; Han, M.; Liu, W.S. Study on the Mechanism of Ionic Stabilizers on Shale Gas Reservoir Mechanics in Northwestern Hunan. *Energies* **2019**, *12*, 2453. [CrossRef]
32. Khalid, P.; Qayyum, F.; Yasin, Q. Data-Driven Sequence Stratigraphy of the Cretaceous Depositional System, Punjab Platform, Pakistan. *Surv. Geophys.* **2014**, *3*, 1065–1088. [CrossRef]

